Effect of temperature cycle on mechanical properties of methane hydrate-bearing sediment

Thi Xiu Le, Patrick Aimedieu, Michel Bornert, Baptiste Chabot, Stéphane Rodts, Anh Minh A.M. Tang

Effect of temperature cycle on mechanical properties of methane hydrate-bearing sediment

Thi Xiu Le, Patrick Aimedieu, Michel Bornert, Baptiste Chabot, Stéphane Rodts, Anh Minh Tang

Laboratoire Navier (UMR8205 IFSTTAR-ENPC-CNRS), Université Paris Est, Marne-la-vallée, France

Corresponding author:

Dr. Anh Minh TANG

Ecole des Ponts ParisTech

6-8 av. Blaise Pascal, Cité Descartes, Champs-sur-Marne

F-77455 Marne – la – Vallée cedex - France

E-mail: anh-minh.tang@enpc.fr

Abstract

In this study, methane hydrate-bearing sand (MHBS) was created in the laboratory following two methods in order to obtain two types of gas hydrate morphology in sandy sediment. The hydrate morphology in the sediment was assessed by measuring the compressional wave velocity combined with models to predict the wave velocities of the sediment containing gas hydrates. The mechanical properties of the MHBS were investigated by triaxial compression tests. The results obtained by the compressional wave velocity show that after saturating the MHBS sediment (created by the excess gas method) with water, the methane hydrates are partly or completely converted from grain contacts to pore spaces depending on the hydrate saturation (ranging from 0 to 50%). A subsequent temperature cycle completes this conversion process for high hydrate saturation. The results obtained with the triaxial compression tests show higher shear strength, a higher secant Young's modulus, and a higher dilation angle at higher hydrate saturation. In addition, the effects of hydrate saturation on the mechanical properties of the MHBS obtained by the two procedures (with and without the thermal cycle) are similar at low hydrate saturation. The effect of gas hydrate morphologies can only be detected in the case where the conversion (and/or redistribution) of gas hydrates from grain contacts to pore spaces is not complete (at high hydrate saturation).

***Key words**: methane hydrate, sand, mechanical behavior, pore habit, rock physics model.*

1. Introduction

Methane hydrates, being solid ice-like compounds of methane and water, form naturally at high pressure and low temperature. Due to the growing energy demand, natural gas hydrates (primarily methane hydrates) are being considered as an alternative energy source (Collett et al., 2009). However, methane hydrate dissociation during borehole drilling and the production process (with heat or depressurization methods) may reduce the strength of the hydrate-bearing sediments and cause failure (Nixon and Grozic, 2007). In addition, slope instability and wide-scale gas venting are the two most important geo-hazards associated with methane hydrate dissociation problems on the sea floor (Collett et al., 2014; Sultan et al., 2004). For these purposes, various studies have been performed to investigate the mechanical behavior of methane hydrate-bearing sediments.

In natural sediments, methane hydrates exist in the form of nodules/chunks, lenses/veins or pore-filling depending on the characteristic particle size and effective stress (Dai et al., 2012; Konno et al., 2015; Masui et al., 2008). After Collett et al. (2009), the majority (90%) of methane hydrates is said to be found in fine-grained sediments in dispersed forms, but hydrate saturation is typically low. On the contrary, the larger pore size and relatively high permeability of sandy sediments facilitate methane hydrate formation as pore-filling with high hydrate saturation. For this reason, methane hydrate-bearing sand (MHBS) is the actual target for potential gas hydrate exploration within the scope of future gas production.

In spite of the various numerical models (Jiang et al., 2014; Pinkert & Grozic, 2014; Sánchez et al., 2017; Uchida et al., 2012), few experimental works exist on the investigation of the mechanical behavior of MHBS. Among the existing experimental studies, few works focus on

intact samples (Masui et al., 2008; Winters et al., 2007; Yoneda et al., 2015, 2017). Almost all the experimental works are concerned with laboratory tests on synthetic samples because of the challenges involved with getting cored intact methane hydrate-bearing sediment samples. With recent advances in core pressure technology (pressure-core analysis and transfer system - PCATs), the temperature and pressure of samples can be maintained within hydrate stability so that mechanical tests on almost undisturbed samples can be done. However, improvements are still needed to increase the successful pressuring core proportion and to efficiently extrude samples into the PCAT's triaxial cell (Priest et al., 2015; Yamamoto, 2015; Yoneda et al., 2017, 2015).

The hydrate morphology in sediments is usually assessed by comparing the measured seismic velocities and those calculated via models (Dvorkin and Nur, 1998, 1996; Helgerud et al., 1999). In the model proposed by Helgerud et al. (1999), four pore-scale hydrate distributions are considered. This model is based on the fact that seismic velocities depend on the bulk elastic moduli of the system, which are controlled by the grain-scale arrangements of the hydrates and the sediment. For a given hydrate saturation, the hydrates floating in the pore fluid (pore-filling morphology) increase the seismic velocity by increasing the modulus of the pore fluid. This has the smallest impact on the host sediment's elastic properties. On the contrary, hydrates forming only at the grain contacts and acting as cement (contact cement morphology) have the greatest impact on the elastic properties of sediments and increase the seismic velocity by locking individual grains together. The hydrates forming part of the sediment frame (load-bearing morphology) are simply considered as a second mineral in the quartz sand pack, while the hydrates surrounding and cementing the sediment grains (grain-coating morphology) are held together by the effective pressure. Their presence dramatically increases the granular contact stiffness by locking the grains in place.

The relationship between compressional velocity and hydrate saturation is usually used to assess the hydrate pore habit. In sandy samples, the gas hydrates can be created at the contacts between the sand grains in gas-saturated media by various methods: (i) ice seeding (Priest et al., 2005), (ii) excess gas (partial water saturation) without water saturation (Grozic and Ghiassian, 2010; Hyodo et al., 2013a; Waite et al., 2004; Winters et al., 2007; Zhang et al., 2012), (iii) or excess gas (partial water saturation) followed by water saturation (Hyodo et al., 2013a; Miyazaki et al., 2011b). Dissolving the gas is considered as a good method for reproducing natural methane gas hydrate formation in marine sediments, but this method is time-consuming especially at high hydrate saturation due to the low solubility of methane gas in water (Spangenberg et al., 2005). Priest et al. (2009) proposed the water excess method, but methane hydrates formed heterogeneously inside their sample (Kneafsey et al., 2010). Choi et al. (2014) proposed a non-cementing methane hydrate-forming method by combining the excess gas method with saline water injection at restricted conditions and a temperature cycle. However, in the work of Choi et al. (2014), mechanical tests were not performed to investigate the effect of the hydrate pore habit (hydrate morphology) on the mechanical properties of the sediment.

Without measuring the acoustic properties, Ebinuma et al. (2005) and Masui et al. (2005) formed methane hydrates by the excess gas and ice-seeding methods, determined the mechanical properties of MHBS (by triaxial compression tests), and suggested that pore-filling hydrates could be created by the ice-seeding method.

In the present work, gas hydrates were created in sandy samples following two methods. The

first one corresponds to the creation of methane hydrates in a partial water saturation sample followed by a water saturation phase prior to the mechanical testing. The second one was similar to the first one, but was completed with a temperature cycle (as suggested by Choi et al., 2014). That would lead to two types of hydrate pore habits. The measurement of the compressional wave velocity and triaxial compression tests were used to assess the grain-scale hydrate distribution in sediments. Tests were performed with various hydrate saturations (0 - 50%) to investigate the effect of this parameter on the mechanical properties of the MHBS. It should be noted that gas hydrate-bearing sandy sediments in nature could have higher hydrate saturation (up to 80%). In addition, other researchers (Yoneda et al., 2017; Yun et al., 2007) mentioned that the mechanical properties of hydrate-bearing sediments would change exponentially with hydrate saturation in the range over 40~50%. However, the hydrate pore habit would be more complex in these cases and would need more extensive work.

2. Experimental method

2.1. Materials

The soil used in this study was Fontainebleau silica sand (NE34). Its mechanical properties are generally well-documented (Dupla et al., 2007). It consists of poor-graded sub-rounded grains having diameters ranging from 100 to 300 microns (the particle size distribution curve shown in Figure 1 was obtained by laser diffraction analysis). Tap water was used in the tests. The standard purity of the methane gas used here was 99.995%.

2.2. Experimental setup

Figure 2 presents a schematic view of the temperature-controlled high-pressure triaxial apparatus. The sample (1) was covered with a neoprene membrane, 50 mm in diameter and 100 mm in height. A displacement sensor (2) was used to monitor the radial strain of the sample, serving to calculate the volumetric strain during consolidation. For the mechanical loading, the

confining pressure was applied to the fluid (silicone oil) inside the cell by a volume/pressure controller (3); the deviator stress, applied via the piston (4), was measured by the force transducer (5) installed above the piston. It should be noted that the friction between the cell and the piston (corresponding to approximately 200 kPa of deviator stress) can be measured when the piston is moved down without touching the top baseplate (10). Methane gas was injected via the bottom inlet (6) by a pressure controller, which was connected to a gas flowmeter. The top and bottom pore pressure transducers were connected by a T-valve (7). The pore water pressure was controlled by a volume/pressure controller (8). For the temperature control, the cell was immersed in a temperature-controlled bath connected with a cryostat. A thermocouple (9) was placed close to the sample to measure the temperature inside the cell. For the measurements of the compressional wave velocities, two ultrasonic sensors were installed on the top and bottom baseplates (10) and connected to a wave generator.

2.3. Test procedure

MHBS samples were prepared by the following procedure:

- Step 1: Moist sand (having a known moisture content) was compacted by tamping in layers to obtain a void ratio of 0.63 inside the neoprene membrane prior to the assembly of the experimental setup, as shown in Figure 2.
- Step 2: The sample was consolidated at drained conditions (state 1 in Figure 3). The confining pressure was increased to 25 MPa then decreased to 10 MPa. As the maximal value of confining pressure during the subsequent test was 22 MPa, the consolidation step would ensure that the soil remained in the elastic domain during the whole test.
- Step 3: To create methane hydrates inside the sample, the temperature of the bath was decreased to 3 – 4°C and vacuum was applied to eliminate the pore air in the sample. Afterward, methane gas was injected at 7 MPa during the whole methane hydrate formation period (state 2 in Figure 3). The methane hydrate formation in gas-saturated

media was considered complete when the methane gas flow rate became negligible (< 0.1 ml/min). At the end of this step, methane hydrate saturation can be estimated from the initial water saturation (an increase in volume of 10% was considered due to the water-hydrate shift). It should be noted that 7 MPa of gas pressure is much higher than the value required to create gas hydrates at a temperature of 3 - 4°C (see state 2 in Figure 3). In addition, preliminary studies have shown that the ultrasonic sensors could correctly measure the compressional wave velocities only in the case of an effective stress higher than 1 MPa (Ebinuma et al., 2008; Rydzy and Batzle, 2010). For this reason, a confining pressure of 10 MPa (corresponding to an effective stress of 3 MPa) was chosen.

- Step 4: To saturate the MHBS sample, the T-valve (7) was opened to the atmosphere for a short period (about 10 s) to let the excess gas (initially under a pressure of 7 MPa) escape from the sample (i.e., the pore pressure decreased to zero) and then this valve was connected to the volume/pressure controller (8) to inject water with a pressure of 7 MPa. This procedure allowed the excess gas to be replaced in the sample by water and minimized the disturbance of methane hydrates that already existed inside the sample by saturating the sample without circulating water.

After the above steps had been completed, two different procedures were used:

- For procedure A, a drained triaxial compression test was performed directly after verifying the good saturation of the sample at 22 MPa of confining pressure and 19 MPa of pore pressure by mean of Skempton's coefficient.
- For procedure B, a temperature cycle was performed beforehand to modify the gas hydrate distribution at the grain scale. For this purpose, the pore pressure and the confining pressure were first decreased from 7 MPa to 4 MPa and from 10 MPa to 7 MPa, respectively. All the drainage valves were then closed and the temperature of the

cell was increased to higher than 20°C. That corresponds to a heating of the sample under undrained conditions in order to progressively dissociate the existing gas hydrates. During this phase, the pore pressure (measured by the pressure transducer) increased progressively because of the heating. A Labview program was used to automatically control the confining pressure (via the volume/pressure controller (3)) in order to maintain the mean effective stress (confining pressure minus pore pressure) at 3 MPa. When the pore pressure reached 19 MPa and the confining pressure reached 22 MPa, the T valve (7) was opened for connection with the volume/pressure controller (8). During this step, the pressure in the volume/pressure controller (8) was maintained at 19 MPa and the volume of water expelled during this heating period was monitored. The gas hydrates were supposed to be totally dissociated when the volume of expelled water had stabilized. After this dissociation phase, gas hydrates were then reformed in the sample by decreasing the temperature of the cell to 3-4°C, while maintaining the pore pressure at 19 MPa (and the confining pressure at 22 MPa). This phase induced an injection of water from the volume/pressure controller (8) to the sample. The hydrate reformation phase was considered to be finished when the volume of injected water had stabilized. After the gas hydrate reformation, a drained triaxial compression test was performed under an effective confining pressure of 3 MPa as in the case of tests using procedure A.

In the pore pressure vs temperature plot (Figure 3), procedure A follows the path (1)-(2)-(3), while procedure B follows the path (1)-(2)-(4)-(3). The axial strain rate for all the triaxial compression tests was fixed at 0.1%/min to ensure the drainage conditions. The final methane hydrate saturation was determined by measuring the volume of methane gas dissociated at the end of the triaxial compression tests.

2.4. Test program

The test program is shown in Table 1. Four tests were performed with procedure A (A1 to A4) and four tests were performed with procedure B (B1 to B4). The moisture content was imposed prior to the sample preparation. The water saturation was calculated from the imposed moisture content, the void ratio obtained after the sample preparation (e = 0.63), and the particle density (ρ_s = 2.65 Mg/m^3). In addition, a reference test was performed, which consisted of compacting dry sand down to a void ratio of 0.63 in the triaxial cell. After the consolidation step (confining pressure was increased to 25 MPa and then decreased to 10 MPa), the sample was saturated with water at a confining pressure of 10 MPa and a water pressure of 7 MPa. Finally, a triaxial compression phase at 22 MPa of confining pressure and 19 MPa of pore pressure was applied as with the other samples. The hydrate saturations shown in Table 1 were determined at the end of the tests from the volume of methane gas dissociated from the sample.

3. Experimental results

3.1. Isotropic consolidation

Figure 4 and Figure 5 show the void ratio (e) and the compressional wave velocity (V_p) versus mean effective stress (p'), respectively, during the consolidation step for all tests (Step 2). The points of the unloading phase correspond to the decrease in confining pressure from 25 MPa to 10 MPa followed by the injection of methane gas at 7 MPa. The compression curves ($e - p'$ plot) show a decrease in void ratio from 0.63 to 0.58-0.59 during the loading path (up to p' = 25 MPa). During the unloading path, the void ratio increases to 0.60 – 0.61 (when p' = 3 MPa). The effect of the moisture content on the compression behavior is not clear; the small discrepancy in the results can be then related to the good repeatability of the experimental procedure.

Unlike the compression curves ($e - p'$ plot), where hysteresis can be observed during the loading/unloading paths, the relationship between V_p and p' shows reversible behavior (Figure 5). Actually, during the loading path when p' increases from 1.6 MPa to 25 MPa (the ultrasonic sensors used in this study could not measure V_p lower than 700 m/s), V_p increases from 750 – 850 m/s to 1400 – 1500 m/s. During the unloading path when p' is decreased to 3 MPa, V_p decreases to 900 – 1000 m/s. The results obtained in the consolidation step confirm that V_p is strongly dependent on the mean effective stress (Zimmer, 2004), whereas it is independent of the void ratio and moisture content. For instance, when p' equals 3 MPa, the void ratio at the loading path is higher than that at the unloading path, but the V_p obtained by the two paths are similar. This can be explained by the small volumetric strain (3%). In addition, the results shown in the $V_p - p'$ plot for all the samples (having various moisture contents) are similar. Actually, the matric suction in sand (few kPa, after Feia *et al.*, 2016) is much smaller than the mean effective stress. All the subsequent measurements of V_p were performed at the same mean effective pressure (3 MPa). The discrepancy on the V_p (around ±50 m/s) can be attributed to the repeatability of the experimental procedure.

3.2. Methane hydrate formation

Figure 6 plots V_p versus elapsed time during the methane hydrate formation (Step 3) in gas-saturated media (the confining pressure was maintained at 10 MPa and the gas pressure at 7 MPa). At the beginning, V_p equals 900 – 1000 m/s, corresponding to p' = 3 MPa. V_p increases slightly during the first minutes and then starts to increase quickly. The first period can be identified as the induction time that is necessary to create the first crystals of methane hydrates (Natarajan et al., 1994). In this study, the induction time is approximately 0.2 h. After the induction time, V_p increases quickly during the next 10 h to progressively reach stabilization. The kinematic of V_p evolution within elapsed time is generally independent of the water saturation. The final value of V_p, however, depends on the initial water saturation and this

dependency will be analyzed later. It should be noted that the flow rate of the gas injection at the beginning was much higher than the limit of the flowmeter. For this reason, the total quantity of injected gas could not be measured by the flowmeter.

Figure 7 shows V_p versus elapsed time during the water saturation (Step 4). It should be noted that time zero corresponds to the beginning of the gas-water shift. For the reference test, V_p increases when the sample is saturated with water. In contrast, for all tests with methane hydrates, replacing the excess methane gas with water decreases V_p.

As mentioned above, for the tests following procedure A, triaxial compression tests were performed after the water saturation (Step 4) at 22 MPa of confining pressure and 19 MPa of pore pressure, while for the tests following procedure B, a heating/cooling cycle was applied beforehand to dissociate and recreate the methane hydrates inside the sample. The results obtained during the heating path (procedure B) are shown in Figure 8. After decreasing the pore pressure from 7 MPa to 4 MPa, all the inlets were closed. Afterward, the sample was heated in undrained conditions inducing the increase in pore pressure. The pore pressure reached 19 MPa when the temperature of the cell reached 20°C. As mentioned above, when the pore pressure reached 19 MPa, the volume/pressure controller (8) was connected to the sample to maintain the pore pressure at 19 MPa, while the temperature of the cell continued to be increased. Figure 8c plots the volume of water (and/or methane gas) expelled during this phase. It varies from 4×10^{-6} m^3 to 15×10^{-6} m^3, which corresponds to 5% and 20%, respectively, of the pore volume. In addition, the sample having the higher initial water saturation (higher hydrate saturation) shows a higher volume of expelled water.

Figure 9 presents pore pressure versus cell temperature during this heating path. The phase diagram (relationship between gas pressure and temperature during the dissociation of methane hydrates) is also plotted (Sloan & Koh, 2008). The results show that during this undrained heating path, the $p - T$ plots closely follow the phase diagram (confirming the presence of methane hydrates in the system, after Kwon et al., 2008). However, at a given pressure, the cell temperature (T) is slightly higher than the corresponding temperature determined by the phase diagram. This can be explained by the partial dissociation of hydrates and the continuous heating process (Figure 8a) where the cell temperature is slightly higher than the sample temperature (see also the schematic view of the cell in Figure 2). The $p - T$ plots would be closer to the phase diagram if the heating rate was smaller.

After this dissociation step, to reform gas hydrates, the pore pressure was maintained at 19 MPa, while the cell temperature was decreased to 3 – 4°C (except for test B2). Figure 10 shows the cell temperature and the volume of water injected into the sample versus the elapsed time during this step. Except for the case of test B4, the volume of water injected into the sample is similar to that expelled (shown in Figure 8c) and reaches stabilization after 100 h. The volume measured in test B4 continues to increase with a constant rate even after 120 h. This was then attributed to a possible leakage in the connection that occurred due to the heating/cooling cycle. For test B2, the temperature was first decreased to 15°C, hydrate reformation started and became remarkable after 2 hours. The temperature was finally set at 3-4°C like in the other tests.

3.2. Compressional wave velocity

Figure 11 shows V_p at different steps during the methane hydrate formation process for all the tests. After the consolidation (Step 2), V_p equals to 900 – 1000 m/s for all the samples, as shown in Figure 5 (corresponding to p' = 3 MPa). After the formation of methane hydrates under the

304 gas-saturated state (Step 3), V_p increases significantly (it equals 2500 – 3500 m/s). In addition,
305 samples having similar water saturation show similar V_p. The subsequent water saturation (Step
306 4) slightly decreases the V_p of the gas-saturated MHBS samples, while it increases the V_p of the
307 reference sample. These values vary in the range of 1800 – 2600 m/s. After the gas hydrate
308 dissociation phase, the V_p of all the four samples for B decreases and approaches the
309 corresponding values obtained by the end of the consolidation (Step 2); they vary between 1000
310 and 1200 m/s. Finally, the re-creation of gas hydrates increases V_p again to the range obtained
311 before the dissociation step (end of Step 4), namely, between 1800 – 2300 m/s.

312

313 The results obtained at the end of the gas hydrate formation in the gas-saturated state (Step 3)
314 are presented in Figure 12 where V_p is plotted versus hydrate saturation. The hydrate saturation
315 was estimated from the initial water saturation and all the water was supposed to be used to
316 create gas hydrates. It should be noted that this figure shows the results for eight tests, but the
317 samples with the same moisture content have the same V_p (as shown in Figure 11). That reveals
318 a good repeatability of the experimental procedure. These results show a clear effect of gas
319 hydrate saturation on V_p. V_p is higher at a higher hydrate saturation; it increases from 900 –
320 1000 m/s at the reference state (without hydrates) to 3500 m/s at S_h = 55%.

321

322 In order to assess the gas hydrate distribution at the grain scale, the models proposed by
323 Helgerud (2001) were used. To predict the gas-saturated MHBS morphology, Helgerud (2001)
324 proposed two contact models using two different schemes: (*i*) gas hydrates are located only at
325 the grain contacts (contact cement) and (*ii*) gas hydrates evenly envelop the grains (grain
326 coating). The parameters used are shown in TTable 2. The results (Figure 12) show that the
327 experimental data obtained in the present work correspond to the zone delimited by these two
328 models. In addition, at low hydrate saturation (S_h = 27%) the experimental data fit the “grain

329 coating" model, while at high hydrate saturation (S_h = 55%), the "contact cement" model is
330 more appropriate. The intermediate values of S_h correspond to the intermediate values of V_p.
331
332 The results corresponding to the water-saturated state are plotted in Figure 13. In this figure,
333 the hydrate saturation was calculated from the quantity of methane gas dissociated at the end
334 of each test (the gas that dissolved in water was ignored). The data obtained after the gas hydrate
335 reformation, with the temperature cycle (only for procedure B), are plotted with closed symbols,
336 while the data obtained without the temperature cycle (for procedure A tests) and before the
337 temperature cycle (for procedure B tests) are plotted with open symbols. It should be noted that,
338 for procedure B, V_p decreases after the temperature cycle in tests B2, B3 and B4, while it
339 remains constant in test B1. Unlike the case of the gas-saturated state, the effect of hydrate
340 saturation is less significant. V_p increases from 1850 m/s for the reference case (without
341 hydrates) to 2500 m/s for S_h = 50%. In addition, the V_p obtained after water saturation (Step 4)
342 is generally higher than that obtained after the dissociation/recreation cycle at a given hydrate
343 saturation.
344
345 In order to assess the gas hydrate distribution of water-saturated MHBS at the grain scale, four
346 models proposed by Helgerud (2001) were used. In addition to the two contact models
347 presented above, a model considering hydrates as fluid components (pore-filling) and another
348 considering hydrates as sediment frame components (load-bearing) were used. The
349 experimental and the models' results are plotted in Figure 13 and show that after water
350 saturation, the V_p data match the "load-bearing" model for some cases and are higher than the
351 predicted value for other cases. After the temperature cycle (procedure B), the experimental
352 data correspond to the pore-filling model, except for test B4 (S_h = 42%), where it is close to the
353 load-bearing model.

3.3. Triaxial compressive properties

The results obtained from the drained triaxial compression tests are shown in Figure 14 where deviator stress (q) and volumetric strain (ε_v) are plotted versus axial strain (ε_a). It should be noted that all these samples were consolidated at 25 MPa of effective pressure prior to being unloaded to 3 MPa. The creation of methane hydrates and triaxial compression were performed at a mean effective stress of 3 MPa. The confining pressure and pore pressure were maintained at 22 MPa and 19 MPa, respectively, via the volume/pressure controller, while the axial strain rate was fixed at 0.1%/min. The volumetric strain was calculated based on the volume of water entering/being expelled from the sample. The results obtained from all the tests are quite similar: (*i*) the deviator increases almost linearly at the beginning, it reaches a peak value at about 2-3% of axial strain and decreases progressively to reach a residual state; (*ii*) the volumetric strain shows small contraction at the beginning and then decreases significantly (dilatation) prior to reaching the residual state at high axial strain (ε_a larger than 10%) where ε_v remains constant. There is almost no difference between the results of the two procedures.

The triaxial compressive properties, determined from the results shown in Figure 14, are plotted in Figure 15 versus hydrate saturation (S_h). The peak strength, q_{max}, corresponds to the maximal value of the deviator (Figure 15a); the residual strength, q_{res}, corresponds to the deviator at the end of the test (Figure 15b). The secant Young's modulus, E_{50}, corresponds to the secant stiffness at 50% of the stress difference (Figure 15c). The dilation angle, ψ, is determined from the change in volumetric strain with respect to the change in shear strain by supposing that it is constant between 2 and 4% of the axial strain (Figure 15d). It is obvious that all these values are higher at a higher methane hydrate saturation.

Figure 16 shows an examination of all test results using Rowe's stress-dilatancy analysis for axial deformations before the peak strength was reached. For triaxial compression test conditions, the model is given by

$$\frac{\sigma'_1}{\sigma'_3} = tan^2\left(\frac{\pi}{4} + \frac{\varphi_{cs}}{2}\right)\left(1 - \frac{\dot{\varepsilon}_v}{\dot{\varepsilon}_1}\right)$$

where σ'_1 and σ'_3 are the major and minor effective stresses, respectively, $\dot{\varepsilon}_v$ and $\dot{\varepsilon}_1$ are the volumetric and major principal strain rates, respectively, and φ_{cs} is the critical state friction angle (Pinkert, 2017a).

All the experimental data are close to the values predicted by the model with φ_{cs} = 25°, except for tests A3 and A4.

4. Discussion

The induction time observed, approximately 0.2 h, is almost independent of the initial moisture content. This is in agreement with the results of Chong et al. (2016) who found an induction time of 0.1-0.8 h for fine sand (0.1 – 0.5 mm) prepared at 75% water saturation. Bagherzadeh et al. (2011) used the magnetic resonance imaging technique to investigate the formation of methane hydrates in an unconsolidated bed of silica sand and found that hydrate formation is not uniform and that the nucleation of hydrate crystals occurs at different times and different positions inside the bed. In addition, the hydrate formation was found to be faster with a lower moisture content and a smaller particle size. In the present work, only one particle size distribution was considered and the water saturation varied in a small range (from 25 to 50%). That would explain the independency of the induction time on the moisture content.

Figure 12 shows that gas hydrates significantly increase the compressional wave velocity at the gas-saturated state. The observation of the water distribution in the unsaturated sand at the pore

scale of Crist et al. (2004) reveals that water can be distributed around the grains as a thin layer (by adsorption) and also at the menisci of the grain contacts (by capillarity). In addition, at low water saturation, the water is mainly distributed at the surface of the grains (because the adsorption suction is much higher than the capillary suction); the volume of water at the menisci becomes dominant only at high water saturation. This was also observed by Riedel et al. (2012) via X-Ray Tomography at various water saturations. The injection of gas hydrates at 7 MPa of pressure and 3 – 4°C of temperature induces the transformation of water into the gas hydrates. The results show that this hydrate formation in gas-saturated media increases the V_p (see Figure 6), and this increase reaches the stabilization state after about 100 h. This stabilization suggests that almost the entire quantity of available water has been transformed into gas hydrates. In addition, the distribution of gas hydrates should be similar to that of water prior to its creation. As a consequence, at a low moisture content (hydrate saturation), the gas hydrates are mainly distributed around the grains, while at a high moisture content (hydrate saturation), the role of the gas hydrates at the grain contacts dominates. This explanation is in agreement with the comparison between the experimental data and Helgerud's model shown in Figure 12. Chaouachi et al. (2015) investigated the formation of Xenon gas hydrates in under-saturated sediments with juvenile water using synchrotron X-ray computed tomographic microscopy. The results showed that the nucleation started at the water-gas interface resulting in an initial gas hydrate film, several micrometers in thickness, and future growth proceeded to form isometric single crystals, 10 – 20 micron in size. In the study of Yoneda et al. (2016), the formation of krypton hydrates in partially saturated sand was observed using micro-focus X-ray computed tomography. The results also confirmed the formation of hydrates from the capillary bridges of wet sand and the patchy initial distribution of water.

After the formation of gas hydrates in gas-saturated state, the subsequent water saturation phase significantly decreases the V_p (Figure 7). Ebinuma et al. (2008) and Kneafsey et al. (2010) observed a similar decrease in sonic velocities when saturating the gas-saturated MHBS with water. Hyodo et al. (2013) compared the mechanical properties of gas-saturated MHBS with those of water-saturated ones (using the same sand under the same stress conditions) and found higher stiffness and higher failure strength for gas-saturated specimens. It should be noted that the procedure applied by Hyodo et al. (2013) to obtain water-saturated MHBS is similar to procedure A used in the present work. These results suggest that water saturation modifies the hydrate distribution at the grain scale; the gas hydrates located at the grain contacts would be progressively converted or/and redistributed into the pore spaces (Choi et al., 2014). In this study, the effect of water injection in gas-saturated hydrate-bearing sediments is investigated at different levels of hydrate saturation. The results shown in Figure 7 and Figure 13 indicate that this process takes longer for higher hydrate saturation. For some specimens (B2, B4, A3, and A4), this transformation was not complete when the subsequent step (triaxial compression for specimens A and heating/cooling cycle for specimens B) was applied. This can be explained by the higher values for V_p than the predicted values of the load-bearing model. In addition, for the two tests following procedure A (A3 and A4), even after waiting a long time for water saturation (to make sure that the MHBS was well saturated with water), the V_p were still higher than the values predicted with the load-bearing model. This can perhaps be explained by the patchy hydrate distribution suggested by Dai et al. (2012) where the bulk stiffness approaches the lower Voigt-Reuss bound at low hydrate saturation and the upper bound at high hydrate saturation due to the mechanical interaction between the hydrate-saturated patches. As aforementioned, the number of tests is not so high, but the procedure was correctly controlled in the laboratory. The repeatability of the tests can be appreciated from the results of the

consolidation step (Step 2), seen in Figure 4 and Figure 5, and the hydrate formation in gas-saturated media (Step 3), seen in Figure 6.

In the present work, methane gas was injected into an unsaturated sand specimen to create a MHBS sample. Afterward, water was injected to saturate the specimen. This procedure is similar to that used by Miyazaki et al. (2011) and Hyodo et al. (2013) to investigate the triaxial compressive properties of artificial MHBS. As the initial distribution of water inside the specimen should be homogenous (partly due the equilibrium of the capillary force), it was expected that the distribution of gas hydrates inside the sample would also be homogenous within this method. However, Kneafsey et al. (2010), using X-ray computed tomography, found that this method produced both well-distributed hydrates and very heterogeneous hydrates. They noted that the heterogeneity in the hydrate saturation (observed in the work of Seol & Kneafsey, 2009) was affected by the initial sample heterogeneity, but not dominated by it. In the present work, as the sand specimen was well compacted, the specimen density was relatively homogenous. As a result, the gas hydrate distribution is expected to be homogenous. Observation by magnetic resonance imaging (MRI) on a sample prepared by the same procedure has confirmed this statement (see Le et al., 2019).

The subsequent heating/cooling cycle aims at dissociating/recreating gas hydrates without disturbing the homogeneity of the hydrate distribution. For this reason, during the heating path, the drainage system was closed during the first period. This condition induced an increase in pore pressure (Figure 8 and Figure 9) mainly due to thermal dilation of water and hydrate dissociation (Kwon et al., 2008). The undrained heating condition was stopped when the pore pressure approached the limit of the pore pressure transducer (20 MPa). A small quantity of water (and dissolved methane gas) was then allowed to be expelled. As the final state (in terms

of pore pressure and temperature) is far outside the phase diagram (Figure 9), the methane hydrates should be completely dissociated at the end of the heating path. During the subsequent cooling path, the pore pressure was maintained at 19 MPa, and the cooling induced the injection of water to the specimen (Figure 10). This corresponds mainly to both the thermal contraction of water and the gas hydrate reformation. The reformation of gas hydrates can be easily identified when the cell temperature remains constant, while the volume of injected water increases abruptly (e.g., at 12 h for test B2).

Choi et al. (2014) formed methane hydrates with the partial water saturation method (excess gas method), injecting saline water at locations just outside of the hydrate stability zone for saline water and doing a temperature cycle. It was concluded that slow saline water injection is the key to initiating the formation of non-cementing hydrates and that the temperature cycle ensured this formation. The V_P after warming was quite high, while the sample was not saturated. The hydrate dissociation was perhaps not completed before the hydrate reformation. This explains why the difference in V_p between after the saline water injection and after the temperature cycle was not obvious. The measurement of V_p at the end of the thermal cycle in the present study is smaller than that obtained after water saturation. In addition, it fits with the pore-filling and load-bearing models. It can then be expected that the heating/cooling cycle allows for the completion of the conversion of the hydrate accumulation habit into the non-cementing type.

The experimental results obtained from the triaxial compression tests show higher values for the maximum deviator stress, secant Young's modulus, residual deviator stress, and dilation angle at a higher hydrate saturation. Hyodo et al. (2013) and Miyazaki et al. (2011) found a similar effect for the hydrate saturation on the maximum deviator stress and secant Young's

modulus while testing the MHBS prepared with a procedure similar to procedure A in the present work. The effect of the methane hydrate saturation on the stiffness and failure strength of MHBS was explained by particle bonding. However, the measurement of V_p in the present work suggests that grain-contact hydrates have been significantly converted into non-grain-contact (non-cementing) types by the end of procedure A, as explained above. In addition, the results obtained by procedure B (where the conversion has already been completed) show a similar effect of the hydrate saturation on the stiffness and failure strength of MHBS. Soga et al. (2006) showed a similar increase in the dilation angle with an increase in the hydrate saturation for natural samples and synthetic samples (partial water saturation method for strong grain contacts and ice-seeding method for weak grain contacts) at 1 MPa of confining pressure. It is obvious that an increase in the hydrate saturation enhances the dilative characteristics of soils, and this increase is more apparent when the hydrate saturation exceeds 30%. Recently, Pinkert (2017a,b) analyzed the experimental data obtained by a procedure similar to procedure A and also concluded that no cohesive effect was found when interpreting the test results under a stress-dilatancy framework.

In the present work, the cohesion and friction angle cannot be determined because only one level of effective confining pressure was used. For this reason, the approach of Pinkert (2017a,b) can be appropriated to give more information about the cohesion. When using the method proposed by Pinkert (2017a) to analyze the data obtained in the present work (Figure 16), the results from tests A3 and A4 are positioned above the other curves. These results then correspond to a significant increase in the degree of cohesion in the samples. This is also in agreement with the results shown in Figure 13 and the above comments in which it is expected that the conversion of gas hydrates from grain contacts to pore spaces is not completed for these two cases. To simulate natural hydrate-bearing sediments, with a range in hydrate saturation of

0-50%, procedure A (without the temperature cycle) could be used when the hydrate saturation is smaller than 40%, while at higher saturation (40-50%), a temperature cycle should be added (procedure B should be used).

Conclusions

Methane hydrate-bearing sand was first created by pressurizing methane gas (at 7 MPa) into an already chilled moistened packed sandy specimen (excess gas method). Following the hydrate formation, water was injected into the sample and the remaining gas was simultaneously bled out. The water pressure was then maintained at 19 MPa (22 MPa of confining pressure) until water was no longer injected into the sample. That corresponds to the end of procedure A for preparing the MHBS specimen. For procedure B, a subsequent heating/cooling cycle was applied in order to completely dissociate the gas hydrates and then recreate them inside the specimen. Measurement of the compressional wave velocity was performed along with these processes, while triaxial compression tests were performed at the end of each procedure. Rock physics models were also compared to the experimental data to assess the grain scale distribution of the gas hydrates at each state. The following conclusions can be drawn:

- Pressurizing methane gas into an already chilled moistened packed sandy specimen creates gas hydrates at the grain contacts. This excess gas method allows for a significant increase in V_p.
- Subsequent water saturation converts (and/or redistributes) the gas hydrates from grain contacts to pore spaces and, as a result, decreases V_p. This process may take several days, depending on the hydrate saturation, and cannot be completed for high hydrate saturation.
- The heating/cooling cycle allows for the completion of the conversion (and/or redistribution) of gas hydrates from grain contacts to pore spaces.

- The effects of hydrate saturation on the mechanical properties of MHBS obtained by the two procedures (with and without thermal cycles) are similar at low hydrate saturation.
- The effect of the grain scale gas hydrate distribution can be detected in the case where the conversion (and/or redistribution) of gas hydrates from grain contacts to pore spaces is not complete.

As the non-cementing habit is actually the most representative case of natural gas hydrate-bearing sandy sediments, the findings of the present work would be helpful for future studies on gas hydrate-bearing sediments in the laboratory. Actually, within procedure A, non-cementing hydrates could be obtained by waiting long enough for the completion of the hydrate conversion from grain contacts to pore spaces in the case of small hydrate saturation. With the heating/cooling cycle (procedure B), non-cementing hydrates could even be obtained at higher hydrate saturation.

Acknowledgements

The authors would like to express their great appreciation to the French National Research Agency for funding the present study, which is part of the project HYDRE "Mechanical behavior of gas-hydrate-bearing sediments" –ANR-15-CE06-0008.

We also would like to express our sincere thanks to Marine Lemaire and Emmanuel Delaure for their technical support.

References

Bagherzadeh, S.A., Moudrakovski, I.L., Ripmeester, J.A., Englezos, P., 2011. Magnetic Resonance Imaging of Gas Hydrate Formation in a Bed of Silica Sand Particles. Energy Fuels 2011 25, 3083–3092. doi:10.1021/ef200399a

571 Chaouachi, M., Falenty, A., Sell, K., Enzmann, F., Kersten, M., Haberth, D., Werner, F.K.,
572 2014. Microstructural evolution of gas hydrates in sedimentary matrices observed with
573 synchrotron X-ray computed tomographicmicroscopy. Geochemistry, Geophys.
574 Geosystems 1009–1020. doi:10.1002/2013GC005162

575 Choi, J.-H., Dai, S., Cha, J.-H., Seol, Y., 2014. Laboratory formation of noncementing hydrates
576 in sandy sediments. Geochemistry, Geophys. Geosystems 15, 1648–1656.
577 doi:10.1002/2014GC005287

578 Chong, Z.R., Yang, M., Khoo, B.C., Linga, P., 2016. Size Effect of Porous Media on Methane
579 Hydrate Formation and Dissociation in an Excess Gas Environment. I&EC Res. 55,
580 7981−7991. doi:10.1021/acs.iecr.5b03908

581 Collett, T., Bahk, J., Baker, R., Boswell, R., Divins, D., Frye, M., Goldberg, D., Husebø, J.,
582 Koh, C., Malone, M., Morell, M., Myers, G., Shipp, C., Torres, M., 2014. Methane
583 Hydrates in Nature - Current Knowledge and Challenges. J. Chem. Eng. data 60, 319–329.

584 Collett, T.S., Johnson, A.H., Knapp, C.C., Boswell, R., 2009. Natural gas hydrates: A review.
585 Am. Assoc. Pet. Geol. 89, 146–219. doi:10.1306/13201101M891602

586 Crist, J.T., McCarthy, J.F., Zevi, Y., Baveye, P.C., Throop, J. A., Steenhuis, T.S., 2004. Pore-
587 Scale Visualization of Colloid Transport and Retention in Partly Saturated Porous Media.
588 Vadose Zo. J. 3, 444–450. doi:10.2113/3.2.444

589 Dai, S., Santamarina, J.C., Waite, W.F., Kneafsey, T.J., 2012. Hydrate morphology: Physical
590 properties of sands with patchy hydrate saturation. J. Geophys. Res. B Solid Earth 117.
591 doi:10.1029/2012JB009667

592 Dupla, J.C., Pedro, L.S., Canou, J., Dormieux, L., 2007. Comportement mécanique de sols
593 grossiers de référence. Bull. des Lab. des Ponts Chaussees 31–57. doi:10.3233/978-1-
594 60750-031-5-64

595 Dvorkin, J., Nur, A., 1998. Acoustic signatures of patchy saturation. Int. J. Solids Struct. 35,
596 4803–4810. doi:10.1016/S0020-7683(98)00095-X

597 Dvorkin, J., Nur, A., 1996. Elasticity of high-porosity sandstones: Theory for two North Sea
598 data sets. Geophysics 61, 890–893. doi:10.1190/1.1444059

599 Ebinuma, T., Suzuki, K., Nagao, J., Oyama, H., Narita, H., Hydrate, M., 2008. OTC 19260
600 Ultrasonic Wave Velocities Associated with Formation and Dissociation of Methane
601 Hydrate in Artificial Sandy Sediment, in: Offshore Technology Conference (OTC).
602 Houston, Texas. doi:10.4043/19260-MS

603 Ebinuma, T., Kamata, Y., Minagawa, H., Ohmura, R., Nagao, J., Narita, H., 2005. Mechanical
604 Properties of Sandy Sediment Containing Methane Hydrate, in: The 5th International
605 Conference on Gas Hydrates. Trondheim, pp. 958–961.

606 Feia, S., Dupla, J.C., Ghabezloo, S., Sulem, J., Canou, J., Onaisi, A., Lescanne, H., Aubry, E.,
607 2015. Experimental investigation of particle suspension injection and permeability
608 impairment in porous media. Geomech. Energy Environ. 3, 24–39.
609 doi:10.1016/j.gete.2015.07.001

610 Grozic, J., Ghiassian, H., 2010. Undrained shear strength of methane hydrate-bearing sand;
611 preliminary laboratory results. Proceeding 6th Can. Permafr. Conf. 63rd Can. Geotech.
612 Conf. 459–466.

613 Helgerud, M.B., 2001. Wave speeds in gas hydrate and sediments containing gas hydrate: a
614 laboratory and modelling study. Dep. Geophys. Stanford University.

615 Helgerud, M.B., Dvorkin, J., Nur, A., 1999. Elastic-wave velocity in marine sediments with gas
616 hy-drates: Effective medium modeling. Geophys. Res. Lett.

617 Hyodo, M., Li, Y., Yoneda, J., Nakata, Y., Yoshimoto, N., Nishimura, A., Song, Y., 2013a.
618 Mechanical behavior of gas-saturated methane hydrate-bearing sediments. J. Geophys.

Res. Solid Earth 118, 5185–5194. doi:10.1002/2013JB010233

Hyodo, M., Yoneda, J., Yoshimoto, N., Nakata, Y., 2013b. Mechanical and dissociation properties of methane hydrate-bearing sand in deep seabed. Soils Found. 53, 299–314. doi:10.1016/j.sandf.2013.02.010

Jiang, M., Chen, H., Tapias, M., Arroyo, M., Fang, R., 2014. Study of mechanical behavior and strain localization of methane hydrate bearing sediments with different saturations by a new DEM model. Comput. Geotech. 57, 122–138. doi:10.1016/j.compgeo.2014.01.012

Kneafsey, T.J., Rees, E.V.L., Nakagawa, S., Kwon, T., 2010. Examination of Hydrate Formation Methods : Trying to Create Representative Samples.

Konno, Y., Yoneda, J., Egawa, K., Ito, T., Jin, Y., Kida, M., Suzuki, K., Fujii, T., Nagao, J., 2015. Permeability of sediment cores from methane hydrate deposit in the Eastern Nankai Trough. Mar. Pet. Geol. 66, 487–495. doi:10.1016/j.marpetgeo.2015.02.020

Kwon, T.H., Cho, G.C., Santamarina, J.C., 2008. Gas hydrate dissociation in sediments: Pressure-temperature evolution. Geochemistry, Geophys. Geosystems 9, 1–14. doi:10.1029/2007GC001920

Le, T.X., Rodts, S., Hautemayou, D., Aimdieu, P., Bornert, M., Chabot, B., Tang, A.M., 2019. Kinetics of methane hydrate formation and dissociation in sand sediment. Geomechanics for Energy and the Environment. doi: 10.1016/j.gete.2018.09.007

Masui, A., Haneda, H., Ogata, Y., Aoki, K., 2005. The effect of saturation degree of methane hydrate on the shear strength of synthetic methane hydrate sediments, in: The 5th International Conference on Gas Hydrates, Trondheim, Norway. Trondheim, pp. 657–663.

Masui, A., Kuniyuki, M., Hironori, H., Yuji, O., Kazuo, A., 2008. Mechanical Properties of Natural Gas Hydrate Bearing Sediments Retrieved from Eastern Nankai Trough, in: Offshore Technology Conference (OTC). Houston, Texas. doi:10.4043/19277-MS

643 Miyazaki, K., Masui, A., Sakamoto, Y., Aoki, K., Tenma, N., Yamaguchi, T., 2011a. Triaxial
644 compressive properties of artificial methane-hydrate-bearing sediment. J. Geophys. Res.
645 Solid Earth 116. doi:10.1029/2010JB008049

646 Miyazaki, K., Tenma, N., Aoki, K., Sakamoto, Y., Yamaguchi, T., 2011b. Effects of confining
647 pressure on mechanical properties of artificial methane-hydrate-bearing sediment in
648 triaxial compression test. Int. J. Offshore Polar Eng. 21, 148–154.

649 Natarajan, V., Bishnoi, P.R., Kalogerakis, N., 1994. Induction phenomena in gas hydrate
650 nucleation. Chem. Eng. Sci. 2509.

651 Nixon, M.F., Grozic, J.L.H., 2007. Submarine slope failure due to gas hydrate dissociation : a
652 preliminary quantification. Can. Geotech. J. 44, 314–325. doi:10.1139/T06-121

653 Pinkert, S., 2017a. Rowe's Stress-Dilatancy Theory for Hydrate-Bearing Sand. Int. J. Geomech.
654 17, 6016008. doi:10.1061/(ASCE)GM.1943-5622.0000682.

655 Pinkert, S., 2017b. The lack of true cohesion in hydrate-bearing sands. Granul. Matter 19, 57.
656 doi:10.1007/s10035-017-0742-5

657 Pinkert, S., Grozic, J.L.H., 2014. Prediction of the mechanical response of hydrate-bearing
658 sands. J. Geophys. Res. Solid Earth 119, 4695–4707. doi:10.1002/2013JB010920

659 Priest, J.A., Best, A.I., Clayton, C.R.I., 2005. A laboratory investigation into the seismic
660 velocities of methane gas hydrate-bearing sand. J. Geophys. Res. B Solid Earth 110, 1–13.
661 doi:10.1029/2004JB003259

662 Priest, J.A., Druce, M., Roberts, J., Schultheiss, P., Nakatsuka, Y., Suzuki, K., 2015. PCATS
663 Triaxial: A new geotechnical apparatus for characterizing pressure cores from the Nankai
664 Trough, Japan. Mar. Pet. Geol. 66, 460–470. doi:10.1016/j.marpetgeo.2014.12.005

665 Priest, J.A., Rees, E.V.L., Clayton, C.R.I., 2009. Influence of gas hydrate morphology on the
666 seismic velocities of sands. J. Geophys. Res. Solid Earth 114. doi:10.1029/2009JB006284

667 Riedel, I., Andò, E., Salager, S., Bésuelle, P., Viggiani, G., 2012. Water Retention Behaviour
668 Explored by X-Ray CT Analysis, in: Unsaturated Soils: Research and Applications. pp.
669 81–88. doi:10.1007/978-3-642-31116-1_11

670 Rydzy, M.B., Batzle, M.L., 2010. Ultrasonic Velocities in Laboratory-Formed Gas Hydrate-
671 Bearing Sediments, in: Symposium on the Application of Geophysics to Engineering and
672 Environmental Problems 2010. Colorado, pp. 615–624. doi:10.4133/1.3445488

673 Sánchez, M., Gai, X., Santamarina, J.C., 2017. A constitutive mechanical model for gas hydrate
674 bearing sediments incorporating inelastic mechanisms. Comput. Geotech. 84, 28–46.
675 doi:10.1016/j.compgeo.2016.11.012

676 Seol, Y., Kneafsey, T.J., 2009. X-ray computed-tomography observations of water flow
677 through anisotropic methane hydrate-bearing sand. J. Pet. Sci. Eng. 66, 121–132.
678 doi:10.1016/j.petrol.2009.01.008

679 Sloan, E.D.J., 2008. Clathrate Hydrates of Natural Gases.

680 Sloan E.D. and Koh C.A., 2007. Clathrate Hydrates of Natural Gases. CRC Press. 752 pages.

681 Soga, K., Ng, M., Lee, S., Klar, A., 2006. Characterisation and engineering properties of
682 methane hydrate soils, in: The 2nd International Workshop on Characterisation and
683 Engineering Properties of Natural Soils. pp. 2591–2642.
684 doi:10.1201/NOE0415426916.ch26

685 Spangenberg, E., Kulenkampff, J., Naumann, R., Erzinger, J., 2005. Pore space hydrate
686 formation in a glass bead sample from methane dissolved in water. Geophys. Res. Lett.
687 doi:10.1029/2005GL024107

688 Sultan, N., Cochonat, P., Foucher, J.P., Mienert, J., 2004. Effect of gas hydrates dissociation on
689 seafloor slope stability. Mar. Geol. 213, 379–401. doi:10.1111/j.1551-6709.2009.01091.x

690 Uchida, S., Soga, K., Yamamoto, K., 2012. Critical state soil constitutive model for methane

691 Uchida, S., Soga, K. and Yamamoto, K. Critical state soil constitutive model for methane
692 hydrate soil. J. Geophys. Res., 117, B03209, doi: 10.1029/2011JB008661

693 hyW., Winters, W.J., Mason, D.H., 2004. Methane hydrate formation in partially water-
694 saturated Ottawa sand. Am. Mineral. 89, 1202–1207.

695 Winters, W.J., Waite, W.F., Mason, D.H., Gilbert, L.Y., Pecher, I.A., 2007. Methane gas
696 hydrate effect on sediment acoustic and strength properties. J. Pet. Sci. Eng. 56, 127–135.
697 doi:10.1016/j.petrol.2006.02.003

698 Yamamoto, K., 2015. Overview and introduction: Pressure core-sampling and analyses in the
699 2012-2013 MH21 offshore test of gas production from methane hydrates in the eastern
700 Nankai Trough. Mar. Pet. Geol. 66, 296–309. doi:10.1016/j.marpetgeo.2015.02.024

701 Yoneda, J., Jin, Y., Katagiri, J., Tenma, N., 2016. Strengthening mechanism of cemented
702 hydrate-bearing sand at microscales. Geophys. Res. Lett. 43, 7442–7450.
703 doi:10.1002/2016GL069951

704 Yoneda, J., Masui, A., Konno, Y., Jin, Y., Egawa, K., Kida, M., Ito, T., Nagao, J., Tenma, N.,
705 2015. Mechanical properties of hydrate-bearing turbidite reservoir in the first gas
706 production test site of the Eastern Nankai Trough. Mar. Pet. Geol. 66, 471–486.
707 doi:10.1016/j.marpetgeo.2015.02.029

708 Yoneda, J., Masui, A., Konno, Y., Jin, Y., Kida, M., Katagiri, J., Nagao, J., Tenma, N., 2017.
709 Pressure-core-based reservoir characterization for geomechanics: Insights from gas
710 hydrate drilling during 2012–2013 at the eastern Nankai Trough. Mar. Pet. Geol. 86, 1–
711 16. doi:10.1016/j.marpetgeo.2017.05.024

712 Yun, T.S., Santamarina, C.J., Ruppel, C., 2007. Mechanical properties of sand, silt, and clay
713 containing tetrahydrofuran hydrate. J. Geophys. Res. Solid Earth 112, 1–13.
714 doi:10.1029/2006JB004484

715 Zhang, X.-H., Lu, X.-B., Zhang, L.-M., Wang, S.-Y., Li, Q.-P., 2012. Experimental study on
716 mechanical properties of methane-hydrate-bearing sediments. Acta Mech. Sin. 28, 1356–
717 1366. doi:10.1007/s10409-012-0142-3

718 Zimmer, M.A., 2004. Seismic velocities in unconsolidated sands: Measurements of pressure,
719 sorting, and compaction effects. Stanford University.

720

721

722 **Table 1. Test program**

Test	Moisture content (%)	Water saturation (%)	Hydrate saturation (%)
Reference	0.0	0	0
A1	6.0	25	21
B1	6.0	25	13
A2	8.5	35	31
B2	8.5	35	34
A3	10.0	42	50
B3	10.0	42	41
A4	12.0	50	48
B4	12.0	50	42

723 **Table 2. Parameters used for Helgerud's model**

Parameter	Value
Bulk modulus of quartz (GPa)	36.6
Shear modulus of quartz (GPa)	45
Bulk modulus of water (GPa)	2.15
Bulk modulus of air (GPa)	0.01
Porosity (-)	0.387
Density of solid grain (Mg/m^3)	2.65
Density of water (Mg/m^3)	1
Density of air (Mg/m^3)	0
Density of methane hydrate (Mg/m^3)	0.9
Bulk modulus of hydrate (GPa)	7.9
Shear modulus of hydrate (GPa)	3.3
Critical porosity (-)	0.387
Number of contacts per grain (-)	4.5

724

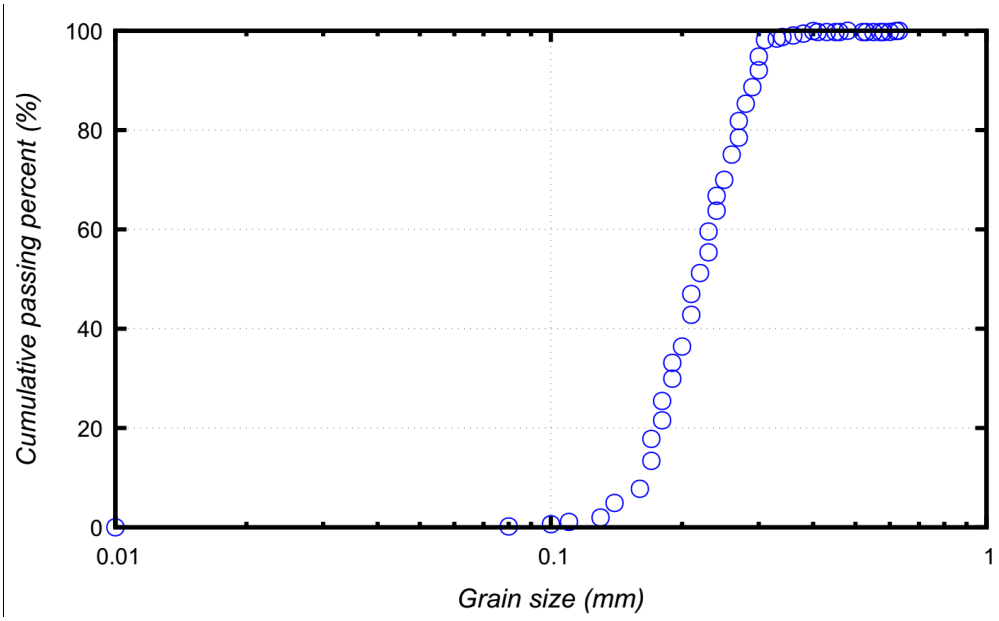

Figure 1. Particle size distribution curve (modified from Feia et al., 2015)

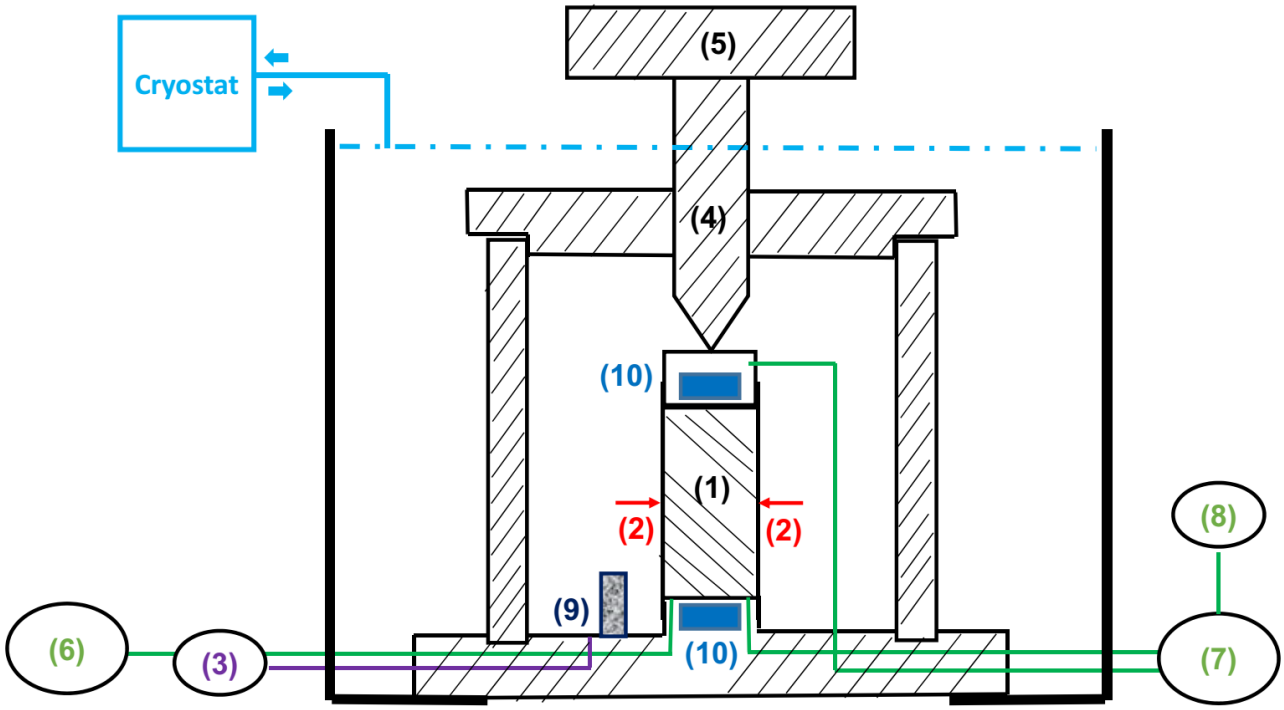

Figure 2. Schematic diagram of the experimental setup

(1): sample; (2): displacement sensor; (3): volume/pressure controller to control confining pressure; (4): piston; (5): force transducer; (6): pressure transducer connected to gas flowmeter for methane gas injection; (7): top and bottom pore pressure transducers connected by a T valve; (8): volume/pressure controller to control pore pressure (water pressure); (9): thermocouple; and (10): two ultrasonic sensors connected to a wave generator for measurement of V_P.

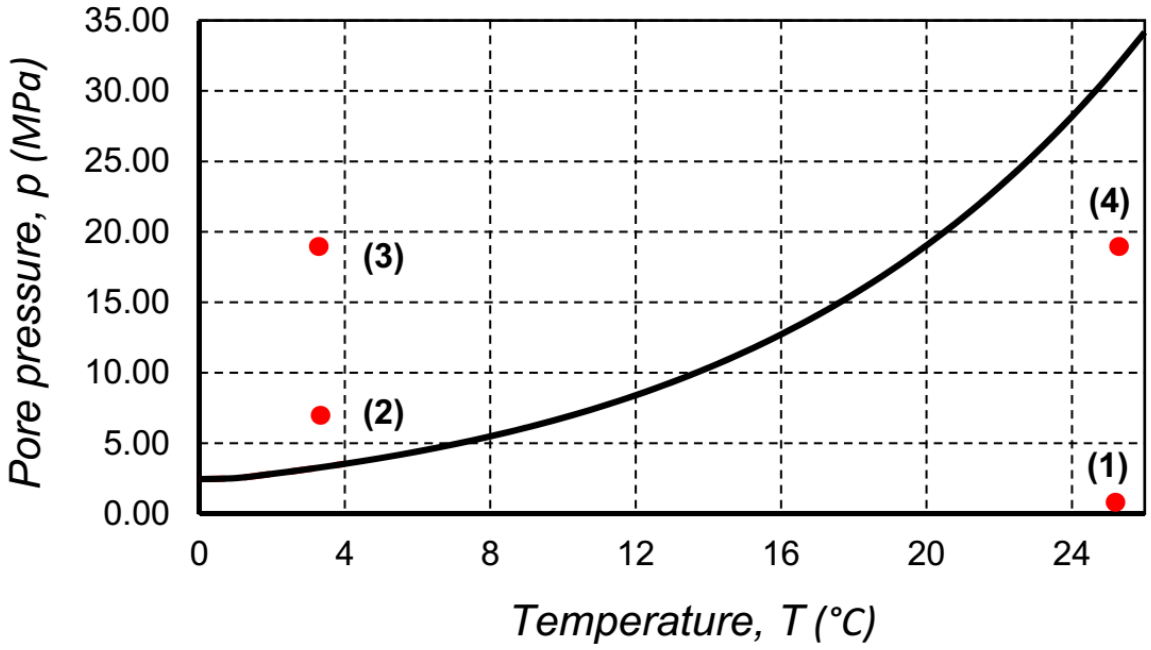

734

735 **Figure 3. *p-T* conditions during gas hydrate formation**

736 (1): Initial state of the sample (Step 1 and Step 2);

737 (2): *p-T* during GH formation in gas-saturated media (Step 3) and after water saturation (Step
738 4);

739 (3):

740 • Procedure A: *p-T* at the end of water saturation when confining pressure and pore
741 pressure were increased to 22 MPa and 19 MPa, respectively;
742 • Procedure B: *p-T* during gas hydrate reformation;

743 (4): *p-T* at the end of gas hydrate dissociation for procedure B tests.

744

745

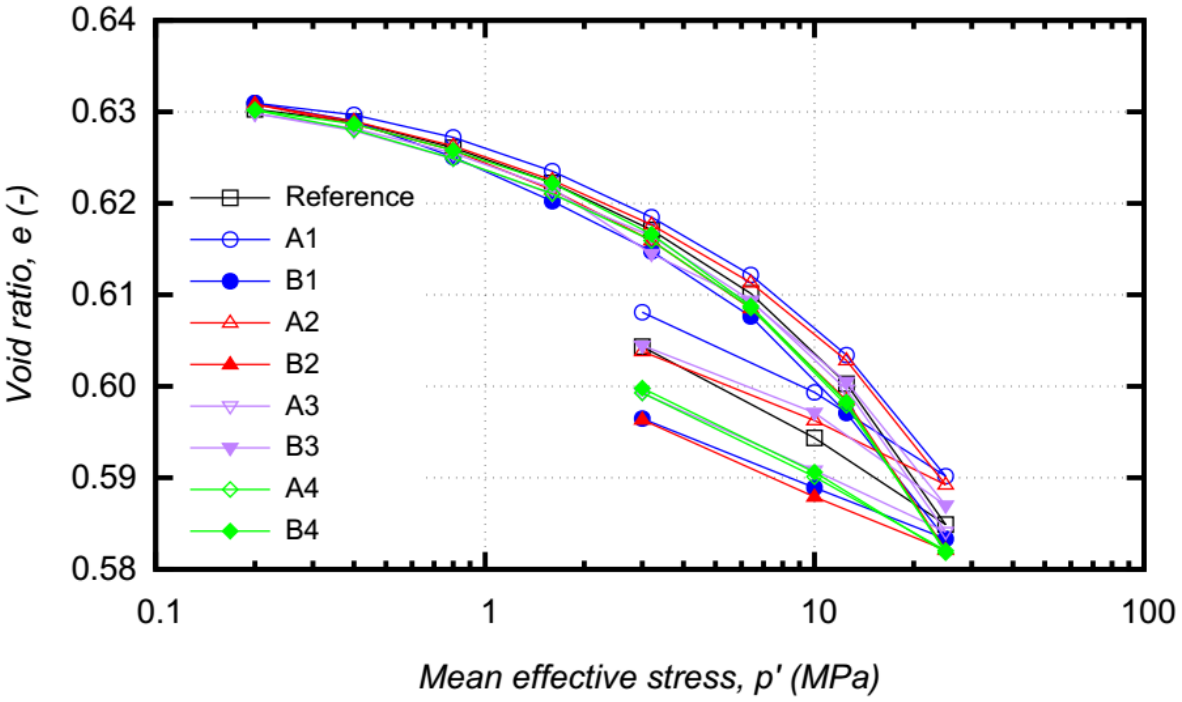

746

747 **Figure 4. Void ratio versus effective stress for all tests**

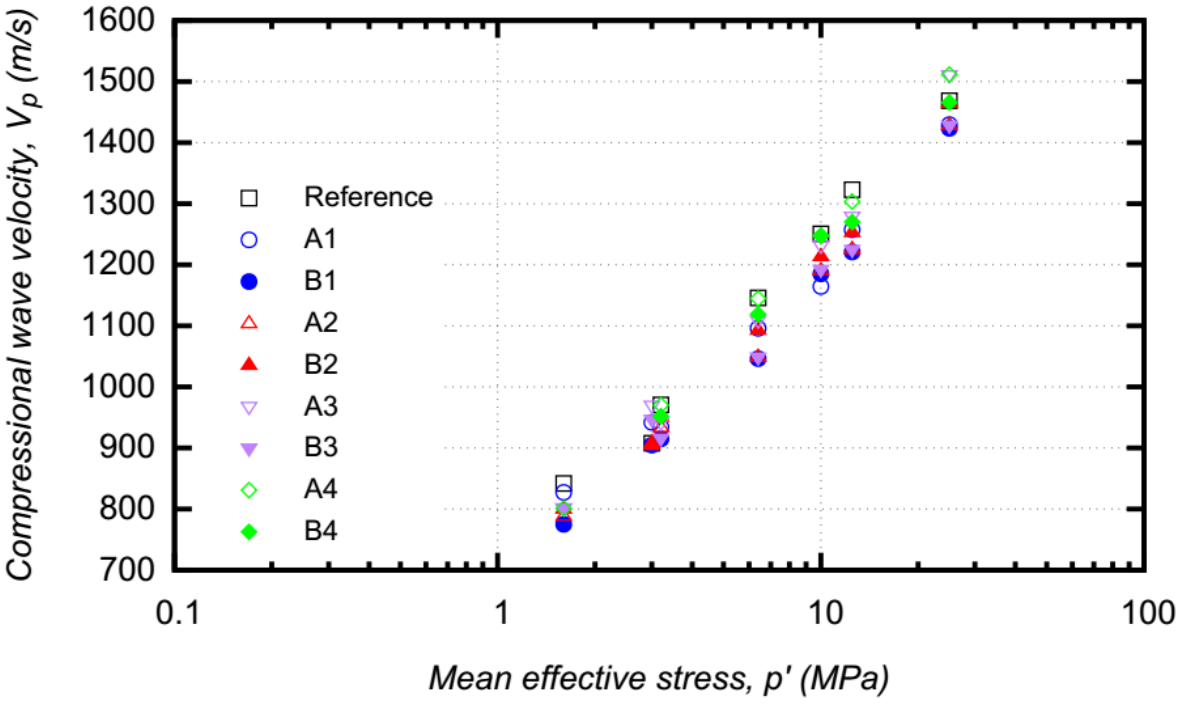

748

749 **Figure 5. Compressional wave velocity versus effective stress for all tests**

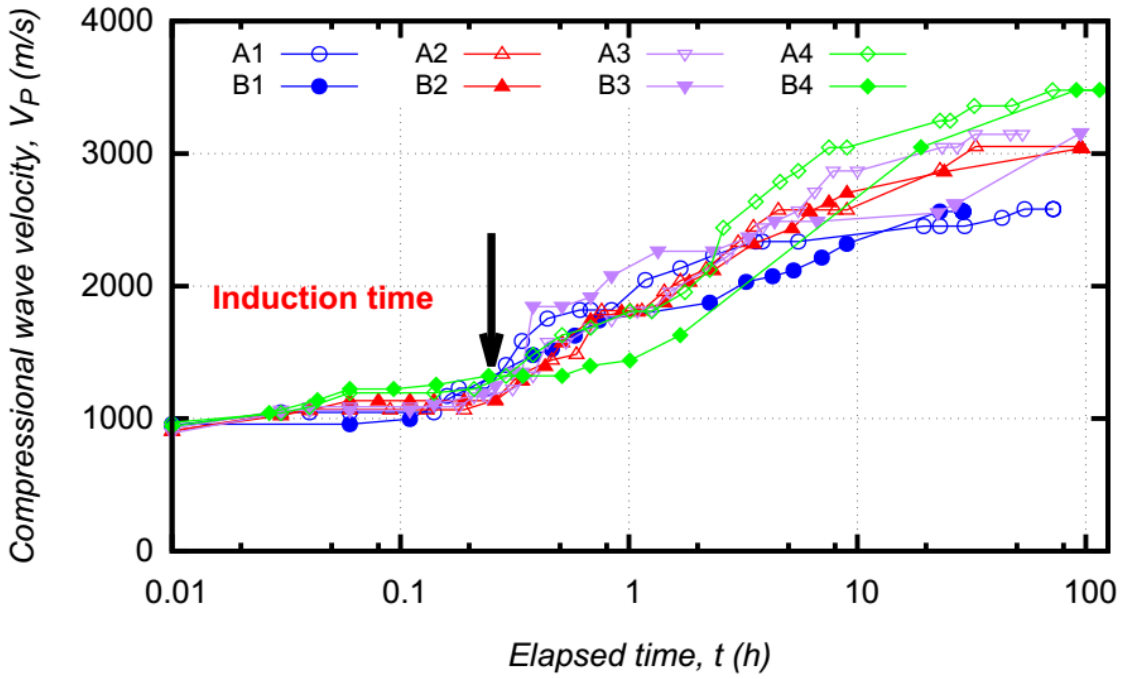

750

751 **Figure 6. Compressional wave velocity versus elapsed time during methane hydrate**
752 **formation in gas-saturated media**

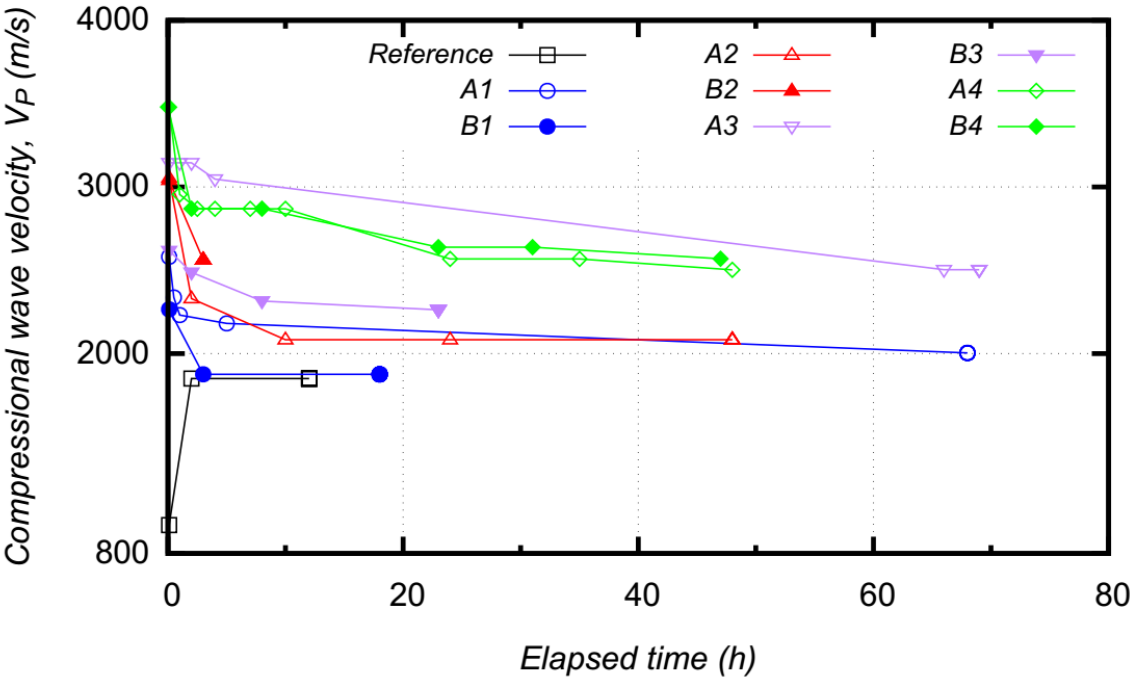

753

754 **Figure 7. Compressional wave velocity versus elapsed time during water saturation**

755

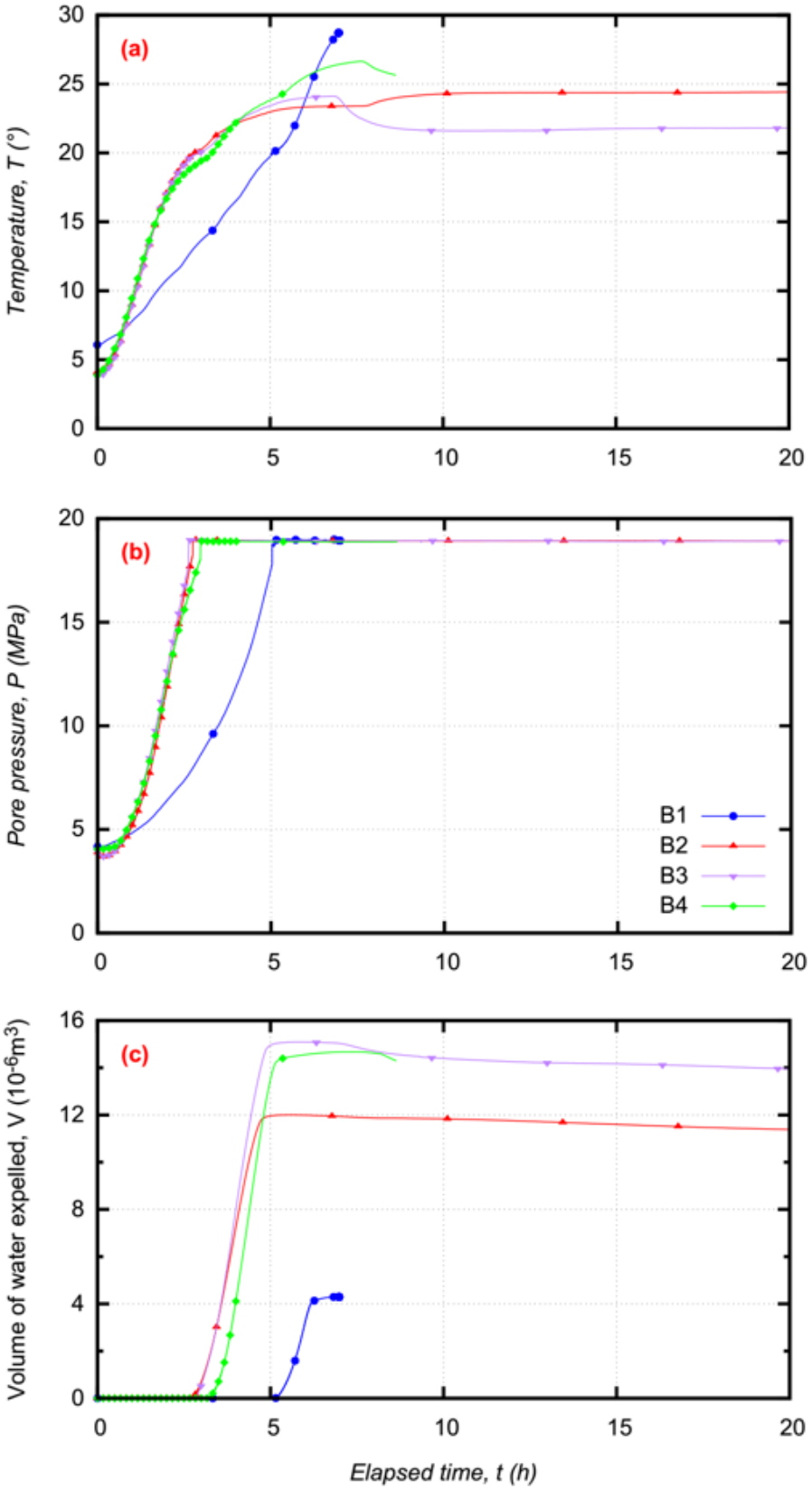

Figure 8. Pore pressure, temperature and volume of water expelled versus elapsed time during heating path

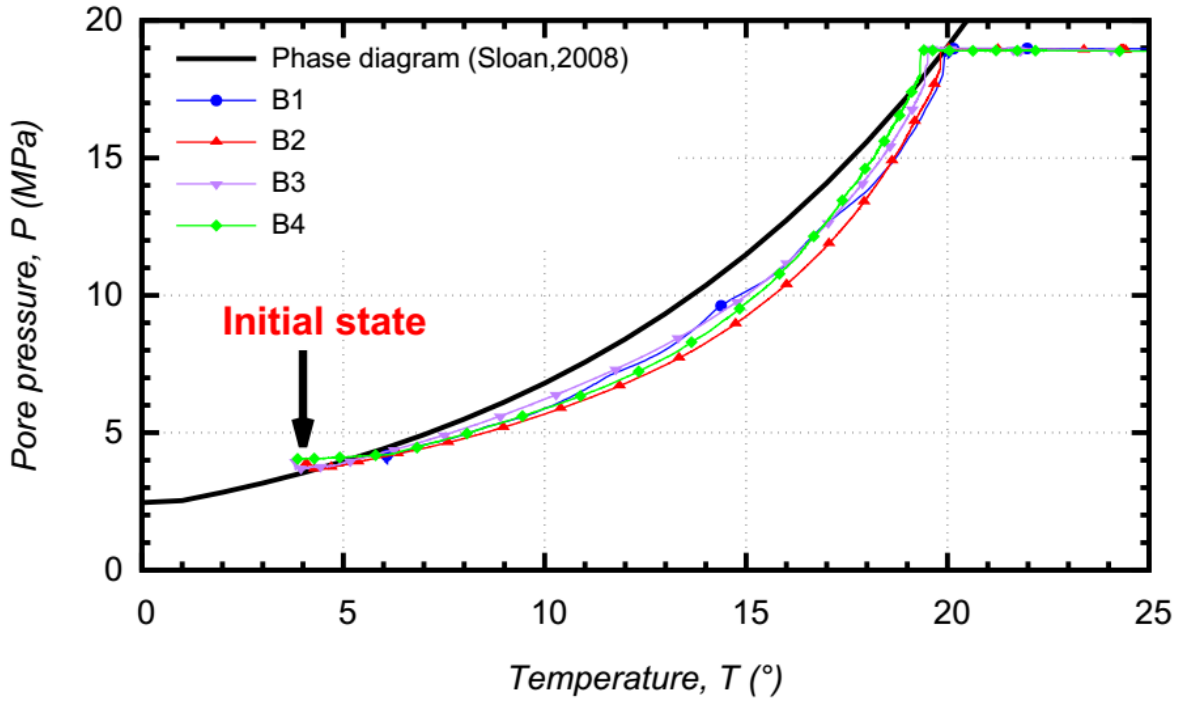

Figure 9. Pore pressure versus cell temperature during dissociation

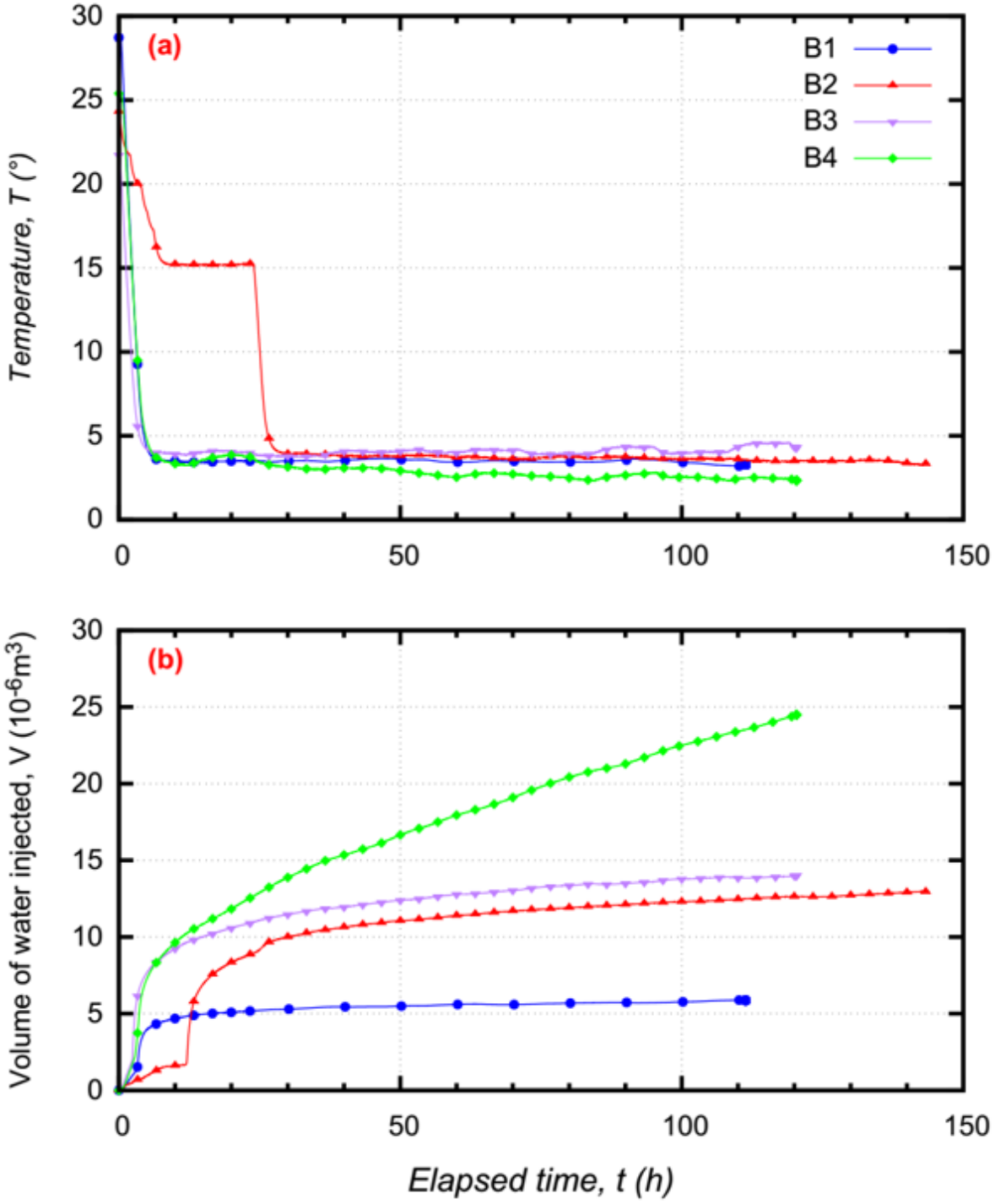

765
766 **Figure 10. Temperature and volume of injected water versus elapsed time during**
767 **hydrate reformation**

768

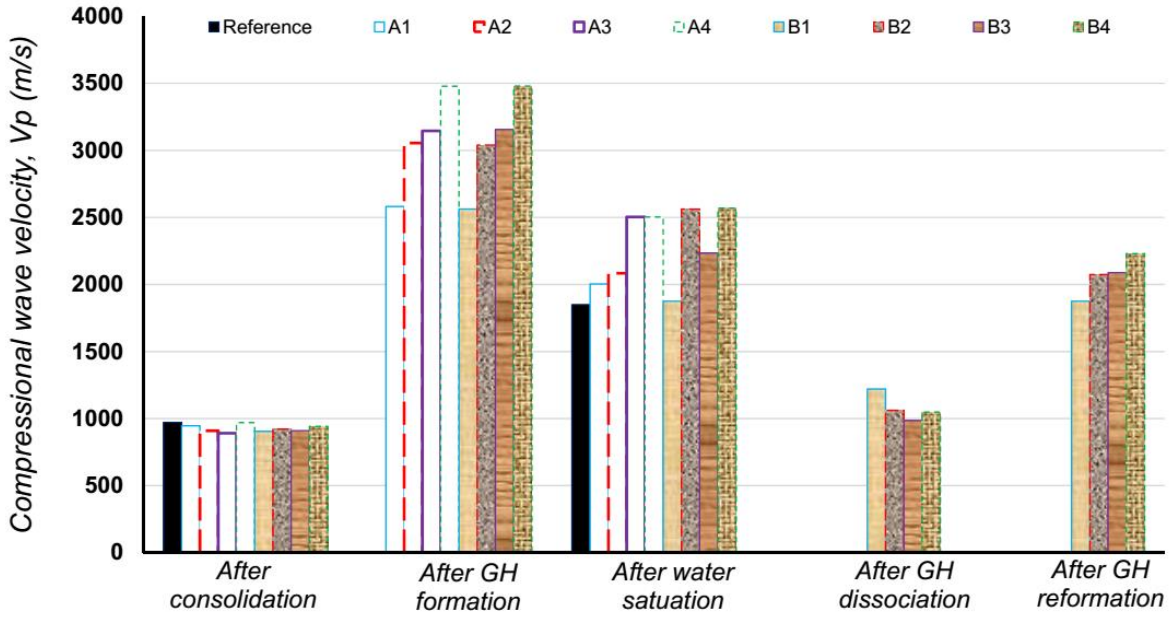

769

770 **Figure 11. Compressional wave velocity during the whole methane hydrate formation of**
771 **all tests**

772

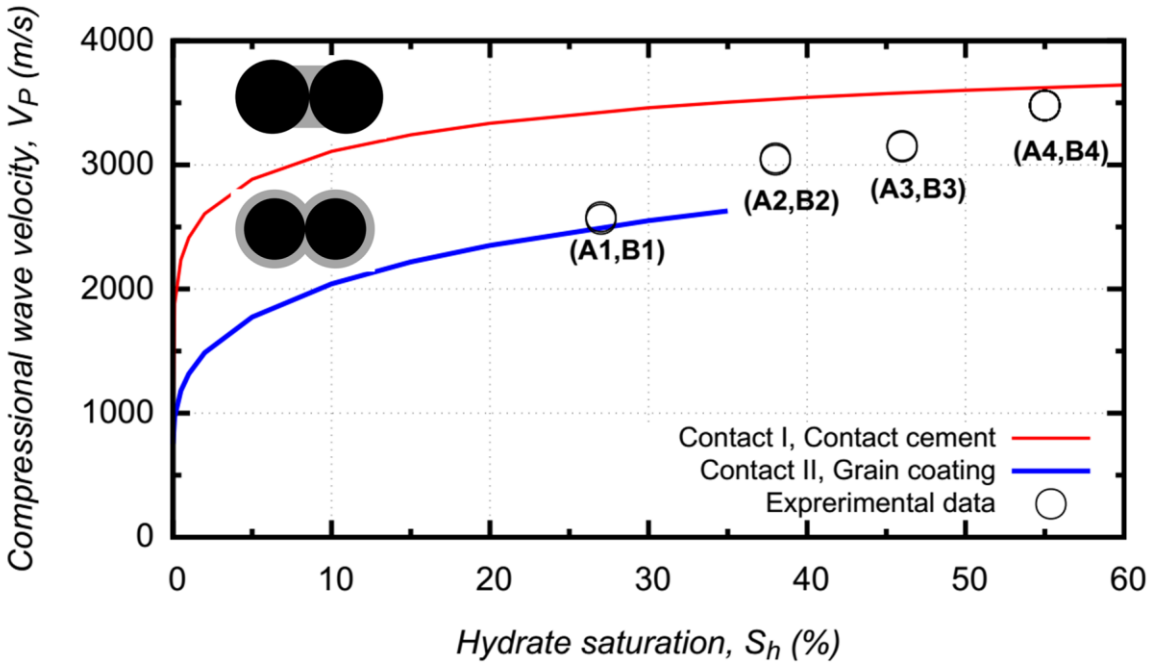

773

774 **Figure 12. Comparison between experiments and Helgerud's model of compressional**
775 **wave velocity dependence on methane hydrate saturation in gas-saturated media**

776

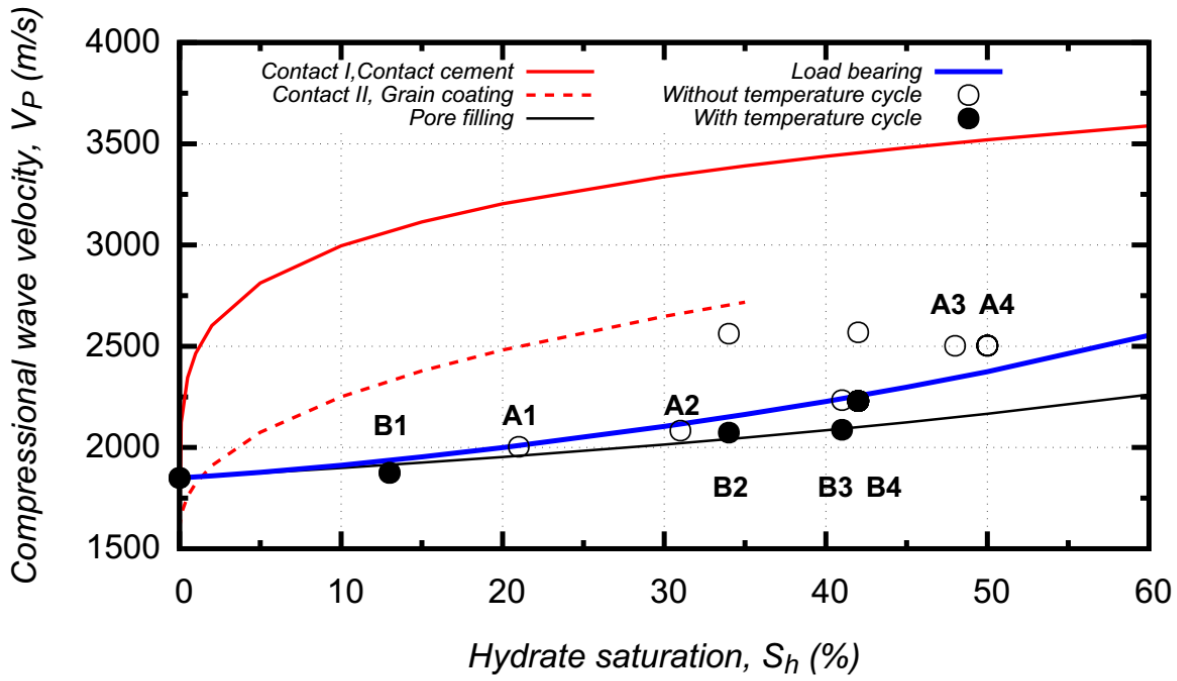

777
778 **Figure 13. Comparison between experiments and Helgerud's model of compressional**
779 **wave velocity dependence on methane hydrate saturation in water-saturated media**

780

781

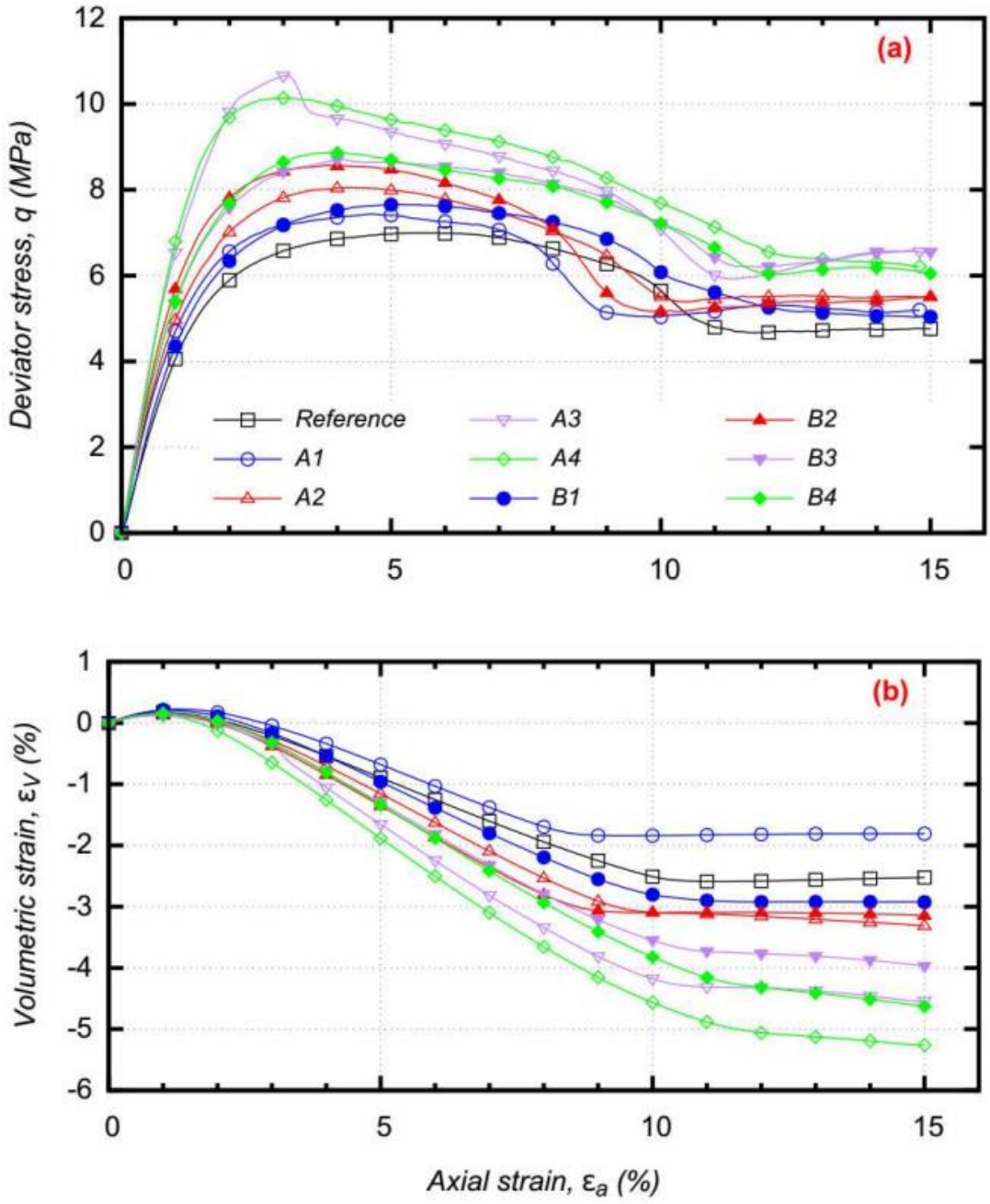

782

783 **Figure 14. Deviator and volumetric strain versus axial strain**

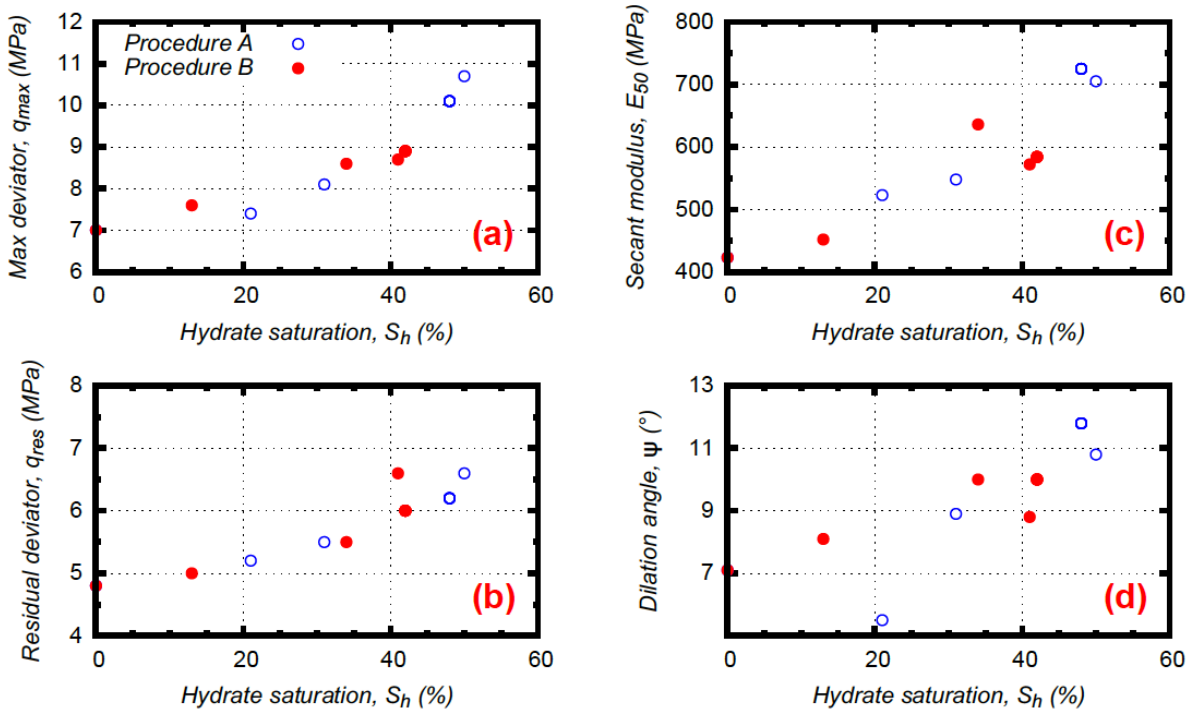

Figure 15. Dependence of mechanical properties of sand on methane hydrate saturation for all tests

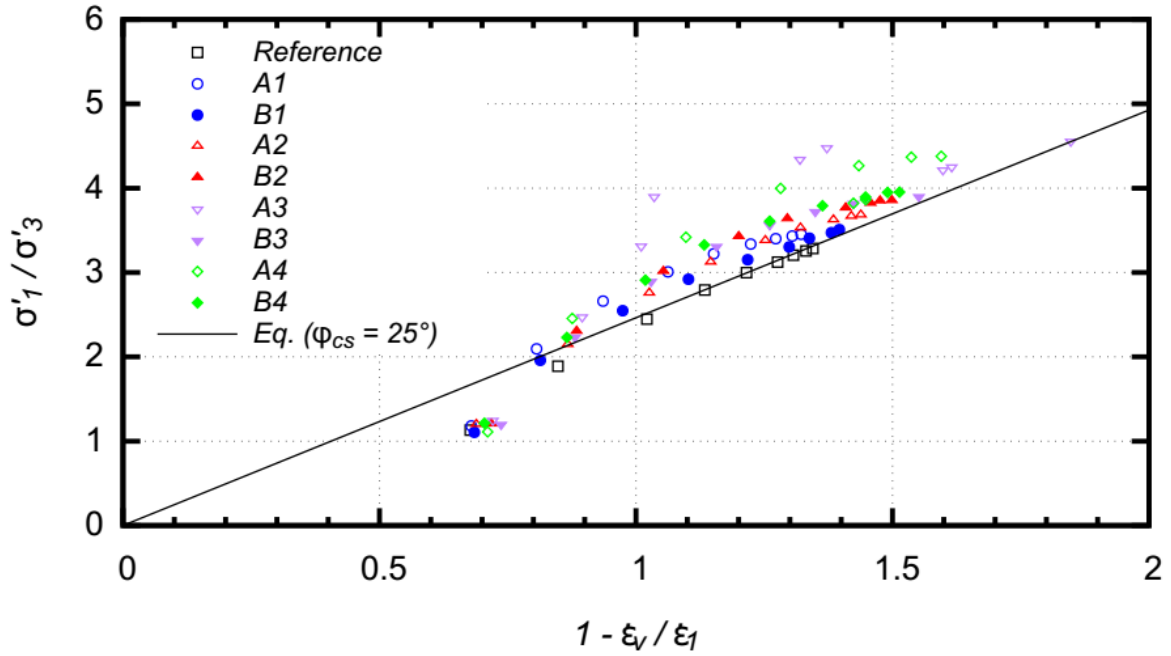

Figure 16. σ'_1/σ'_3 versus 1 - $\dot{\varepsilon}_v/\dot{\varepsilon}_1$